

基于深度相位估计网络的涡旋光束相位校正

刘娟, 杜乾, 刘芳宁, 王珂, 余佳益**, 魏冬梅*

山东师范大学物理与电子科学学院光场调控及应用中心, 山东 济南 250358

摘要 大气湍流会引起涡旋光束(VB)的相位畸变和模态扩散,造成湍流介质中通信性能下降。提出基于深度相位估计网络的拉盖尔-高斯(LG)光束相位补偿方法,以提高模态检测准确度,即通信的可靠性。分别利用使用和不使用高斯光作为探测光束两种方案进行学习,在光强图像与大气湍流引起的扰动相位之间建立映射关系,在接收端依据接收到的光强图像,预测湍流引起的扰动相位并进行相位校正。结果表明,所提深度网络能够较准确地实现相位预测,经补偿后,光束模态纯度达到95%以上,补偿后光强图像与发送端光强图像之间的均方误差明显减小。

关键词 大气光学; 涡旋光束; 卷积神经网络; 相位预测; 大气湍流

中图分类号 TN929.12

文献标志码 A

DOI: 10.3788/AOS221804

1 引言

涡旋光束(VB)具有螺旋相位波前 $\exp(i\theta)$ (其中 i 为虚数单位, θ 为方向角, l 为拓扑荷数), l 直接决定了光束携带的轨道角动量(OAM)的大小,被称为涡旋光束的模态值^[1-2]。理论上,模态值 l 可以无限大,而且不同模态的涡旋光束之间具有正交性^[3],因此,在光通信中,可以利用OAM实现信息传输和交换,也可以对OAM进行复用,提高通信容量^[4-6]。

涡旋光束在大气湍流(AT)中传输时受到湍流影响,导致其螺旋相位失真,造成模间串扰,引起通信可靠性降低^[7-9]。为降低这一湍流的负面影响,目前有许多工作致力于补偿涡旋光束的相位失真,常用的方法是自适应光学系统,如Gerchberg-Saxton算法^[10-11]和随机并行梯度下降算法^[12-14]。但这类方法需要多次迭代,收敛速度较慢,容易陷入局部极小值。

近年来,卷积神经网络(CNN)被引入涡旋光模态检测^[15-18]。在接收端,利用CNN建立光强图样或干涉图样与模态之间的映射关系,实现OAM模态的有效识别,降低OAM解调和复用的技术难度,提高模态检测的准确性^[19],进而提高通信的可靠性。例如,Hao等^[20]建立6层CNN以对单OAM模态进行识别,在大气折射率结构常数 $C_n^2=1\times 10^{-14}\text{ m}^{-2/3}$ 、传输距离为5 km时,识别正确率达到80%。Wang等^[21]基于CNN理论提出了一种6层CNN结构,在 $C_n^2=1\times 10^{-14}\text{ m}^{-2/3}$

传输距离为2 km时,对叠加OAM模态进行识别,识别正确率达到96.25%。如果在模态检测识别前,先对失真相位进行校正,用校正后的光强图进行模态检测,可以提高模态检测的准确度。Liu等^[22]利用高斯探测光束对大气湍流相位进行预测,实现对涡旋光束的校正。校正后,在 $C_n^2=1\times 10^{-13}\text{ m}^{-2/3}$ 、传输距离为20 m时,模态纯度从39.52%提高到98.34%,信道中传输信号的误码率降低了近两个数量级。Xiong等^[23]通过CNN直接从涡旋光束中学习相位映射,对涡旋光束进行补偿校正。在 $C_n^2=5\times 10^{-13}\text{ m}^{-2/3}$ 、传输距离为50 m的情况下,涡旋光束的模态纯度从26.91%提高到93.12%,误码率降低了三个数量级。

上述两种方案,不管是采用高斯光束还是拉盖尔-高斯(LG)光束作为研究对象进行传输,其传输距离都较短。本文利用CNN研究传输较长距离时失真涡旋光束相位补偿效果。

2 涡旋光束在大气湍流中的传输

大气湍流在时间和空间上是连续分布的,在模拟仿真中,光束在大气中的传输可以看作光束在多个具有固定间隔的随机相位屏之间进行传输的光束,如图1所示。

本文中采用Hill-Andrews模型描述大气折射率功率谱^[24-25]:

收稿日期: 2022-10-10; 修回日期: 2022-11-07; 录用日期: 2022-11-22; 网络首发日期: 2022-12-02

基金项目: 国家自然科学基金面上项目(42271093)、国家自然科学基金青年基金(12004218)、山东省本科教学改革项目(2021BJ055)

通信作者: *weidongmei@sdnu.edu.cn; **jiayiyu0528@sdnu.edu.cn

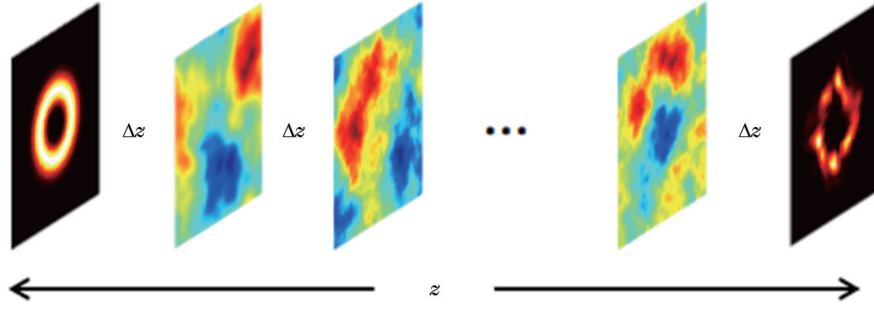


图 1 光波经过多相位屏传输的示意图

Fig. 1 Schematic diagram of beam transmission through multiple phase screens

$$\Phi_n(k_x, k_y) = 0.033C_n^2 \left[1 + 1.802 \sqrt{\frac{k_x^2 + k_y^2}{k_l^2}} - 0.254 \left(\frac{k_x^2 + k_y^2}{k_l^2} \right)^{7/12} \right] \exp \left(- \frac{k_x^2 + k_y^2}{k_l^2} \right) \left(k_x^2 + k_y^2 + \frac{1}{L_0^2} \right)^{-11/6}, \quad (1)$$

式中： k_x, k_y 分别表示 x, y 方向的波数； $k_l = 3.3/l_0$ ， l_0, L_0 分别表示湍流的内、外尺寸。采用功率谱反演法^[26]生成模拟的随机湍流相位屏 $\varphi(x, y)$ ：

$$\varphi(x, y) = \text{FFT}^{-1} \left[C \cdot \sqrt{\left(\frac{2\pi}{N\Delta L} \right)^2 2\pi k_0^2 \Delta z \Phi_n(k_x, k_y)} \right], \quad (2)$$

式中： Δz 为湍流长度； k_0 为波数； ΔL 为接收屏栅格距离；相位屏分辨率为 $N \times N$ ； FFT^{-1} 为傅里叶逆变换； C 为均值为 0、方差为 1 的复随机数矩阵。

设光束的电场函数为 $U(z, x, y)$ ，光束传输 Δz 后，大气湍流引起的扰动相位为 $\varphi(x, y)$ ，根据菲涅耳原理，其电场函数可表示为

$$U(z + \Delta z, x, y) \approx \text{FFT}^{-1} \left\{ \exp \left(-i\Delta z \frac{k_x^2 + k_y^2}{2k_0} \right) \times \text{FFT} [U(z, x, y)] \right\} \times \exp [i\varphi(x, y)], \quad (3)$$

式中： $\exp \left(-i\Delta z \frac{k_x^2 + k_y^2}{2k_0} \right)$ 为菲涅耳传输函数； FFT 为傅里叶变换。

采用 LG 光束进行信息传输，在柱坐标系下，沿 z 轴传输的复振幅可以表示为

$$U_{p,l}(r, \phi, z) = \sqrt{\frac{2p!}{\pi(p+|l|)!}} \frac{1}{w(z)} \left[\frac{r\sqrt{2}}{w(z)} \right]^{|l|} L_p^{(|l|)} \left[\frac{2r^2}{w^2(z)} \right] \exp \left[\frac{-r^2}{w^2(z)} \right] \times \exp(-il\phi) \exp \left[\frac{ik_0 r^2 z}{2(z^2 + z_R^2)} \right] \exp \left[-i(2p + |l| + 1) \arctan \left(\frac{z}{z_R} \right) \right], \quad (4)$$

式中： r 为径向坐标； p 表示径向指数； w_0 表示束腰半径； $z_R = \pi w_0^2 / \lambda$ 表示瑞利长度， λ 为波长； $w(z) = w_0 \sqrt{1 + (z/z_R)^2}$ 表示光斑尺寸； $L_p^{(|l|)}$ 表示拉盖尔多项式； $(2p + |l| + 1) \arctan(z/z_R)$ 表示古伊相位； ϕ 为方位角。图 2 为一个随机模拟相位图。

图 3 为大气湍流对光束传输的影响。图 3(a)~(d) 分别为 $l = 2, 4, 6$ 的 LG 光束经过不同湍流强度 ($C_n^2 = 0, 1 \times 10^{-14}, 5 \times 10^{-14}, 1 \times 10^{-13} \text{ m}^{-2/3}$) 后的光强分布图。从图 3 可以看到，无湍流时，LG 为标准的圆环状。经过湍流传输后，强度分布发生变化。畸变程度随 C_n^2 的增大而增大，OAM 模态发生弥散。本文采用模态纯度 P_m ^[27] 描述模态扩散的程度，则 P_m 可以表示为

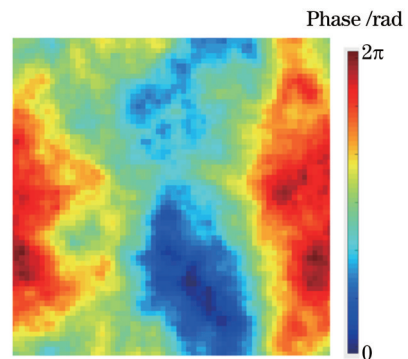


图 2 模拟相位图

Fig. 2 Simulated phase diagram

$$a_m(r, z) = \frac{1}{\sqrt{2\pi}} \sum_{m=-\infty}^{\infty} U(r, \phi, z) \exp(-im\phi) d\phi, \quad (5)$$

$$P_m = \frac{\int_0^{\infty} |a_m(r, z)|^2 r dr}{\sum_{q=-\infty}^{\infty} \int_0^{\infty} |a_q(r, z)|^2 r dr}, \quad (6)$$

式中: $a_m(r, z)$ 为 OAM 模式的概率密度; m 为所求 OAM 的模态值; $U(r, \phi, z)$ 为所求 OAM 光束的电场。

图 4 给出了拓扑荷 $l=5$ 在三种湍流强度下的模态纯度。随着 C_n^2 的增大, 模态纯度从 75.7% 降低到 20.1%。

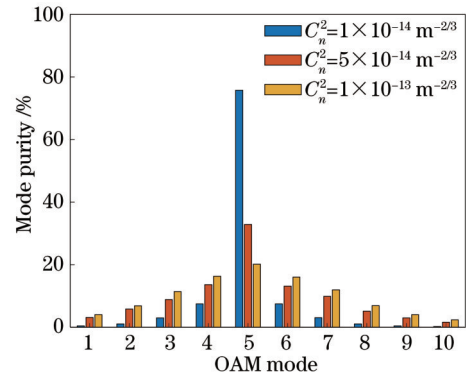


图 4 不同湍流强度下 LG ($l=5$) 的模态纯度

Fig. 4 Mode purity of LG ($l=5$) under different turbulence intensities

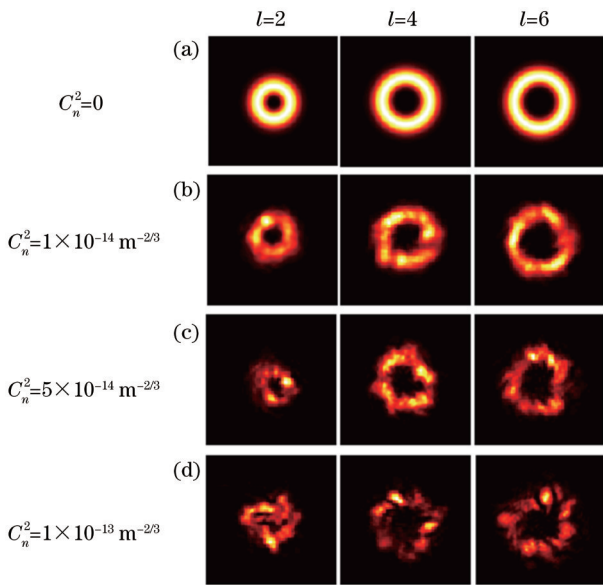


图 3 大气湍流对光束传输的影响

Fig. 3 Influence of atmospheric turbulence on beam transmission

3 深度相位估计网络及相位补偿算法

Lohani 等^[28] 通过一个 5 层 CNN 和梯度下降优化算法进行相位预测, 将预测出来的相位反馈到发射机处, 通过在原空间光调制器上减去预测相位的方法, 完成预补偿, 然后通过湍流传播, 此时, 接收端接收到相位校正后的图像如图 5(a) 所示。Hou 等^[29] 提出一种基于机器学习的两级相位控制方法补偿相位调制器的相位误差, 生成高纯度、高功率、可快速编程控制模态的涡旋光束。

Liu 等^[22-30] 用光强图和 CNN 预测湍流引起的相位, 通过在空间光调制器上加载预测相位的相反相位实现相位补偿, 如图 5(b) 所示。本文采用图 5(b) 所示的补偿方法进行相位补偿, 以达到校正效果。图中 GB 表示高斯光束, AT 表示大气湍流, SLM 表示空间光调制器。

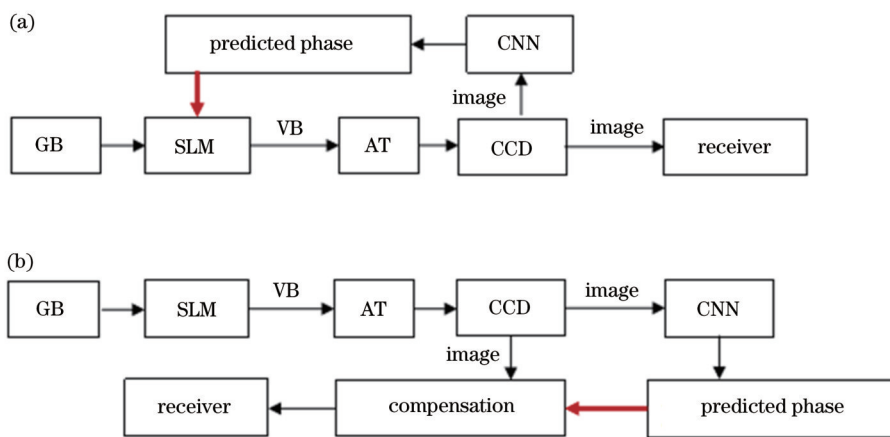


图 5 相位补偿过程框图。(a) 源端预补偿; (b) 接收端直接补偿

Fig. 5 Block diagrams of phase compensation process. (a) Source pre-compensation; (b) direct compensation at receiving end

3.1 网络结构

本文构造如图 6 所示的深度相位估计网络 (DPENet), 实现相位预测。网络包括 15 个卷积层和 3 个反卷积层, 采用编码器解码器架构。其中网络的前

8 层组成编码器, 完成下采样, 得到特征图。第 9 层到 18 层组成解码器, 完成上采样, 将特征图恢复到原图像的分辨率。为更好地恢复图像, 使用跳跃连接, 以拼接方式将解码器和编码器具有相同分辨率的特征图进

行特征融合,拼接后的特征图通道数是原来的 2 倍。如将第 6 层 256 通道的特征图和第 9 层 256 通道的特征图拼接,拼接后得到通道数为 512 的特征图。

在编码器部分,网络输入 128×128 大小的二维灰度光强图像,输入图像经过 8 次卷积和 3 次池化后,得到通道数为 512 的 16×16 大小的特征图。在卷积层中,将输入矩阵与特定特征检测器(也称为核)进行卷积。将图像与核进行卷积,生成一个新的矩阵,称为特征图。每个核可以提取图像的特定特征,不同的核可以提取不同的特征。生成的特征图可作为卷积层的输出,进入下一层。除最后一层外,所有卷积核大小均为 3×3 。特征图进入池化层池化,选择 2×2 的最大池化。池单元从卷积特征图中的每个非重叠 2×2 的子区域获取输入,并选择每个子区域的最大值作为输出,使计算复杂度大大降低。在解码器部分,特征图经过 7 次卷积和 3 次反卷积,输出预测图像,在最后一层使用 1×1 的卷积核将通道数恢复为

1,网络最终输出 128×128 的预测相位图像。反卷积操作可以看作卷积的逆操作,进行卷积操作后,输出特征图尺寸变小,而进行反卷积操作后,输出特征图尺寸大于输入图像尺寸。在整个网络中,将训练数据集等分为多个批次,以提高收敛的稳定性。在每个卷积层后面连接一个批归一化层,实现输入图像的归一化并减少网络训练时间。使用修正线性单元(ReLU 函数)进行非线性激活,防止梯度消失或爆炸,进而加快训练速度。

使用均方误差(MSE)作为损耗函数来进行损失计算,损耗函数为

$$L(\hat{\varphi}_j|\varphi_j) = \frac{1}{n} \sum_{j=1}^n (\hat{\varphi}_j - \varphi_j)^2, \quad (7)$$

式中: $\hat{\varphi}_j$ 是网络输出的预测相位; φ_j 是真实相位; n 为批次大小。使用自适应矩估计优化器将模型损耗最小化,以 10^{-4} 的学习速度进行训练。当迭代次数足够时,网络可以预测出与真实相位高度一致的相位图像。

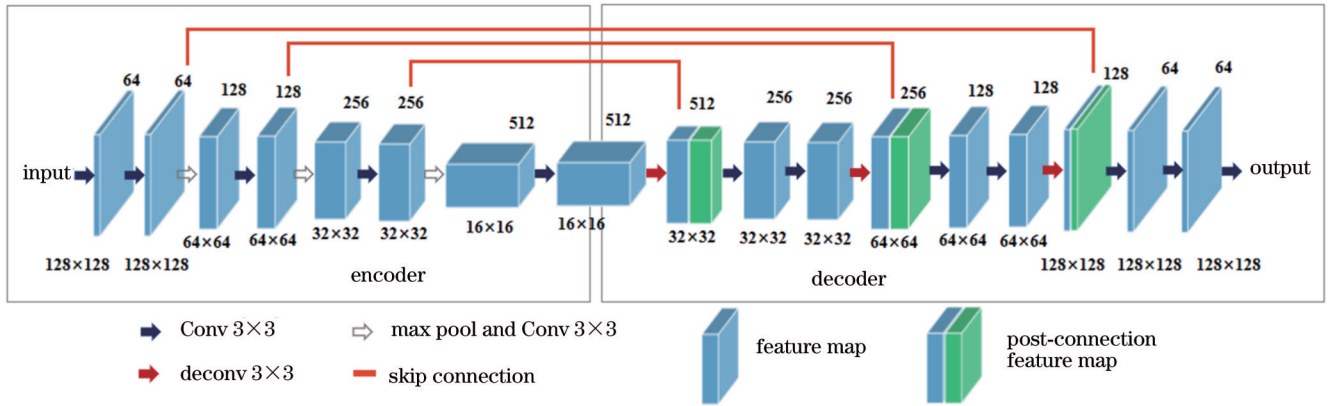


图 6 DPENet 网络结构图

Fig. 6 DPENet network structure

3.2 网络训练

本文采用两种方案进行相位预测,第一种直接使用携带有信息的 LG 进行相位预测,第二种方案使用不携带信息的高斯光束作为探测光束进行训练和预测,并对 LG 光束进行相位补偿和校正,两种方案采用特性完全相同的大气湍流。每一种方案均模拟生成 30000 对样本 (x_j, φ_j) ($j=1, 2, 3, \dots, 30000$) 进行训练。在第一种方案中, x_j 为两种 LG 光强图(受湍流影响和没有受湍流影响),第二种方案 x_j 为两种 GB 光强图(受湍流影响和没有受湍流影响), φ_j 是由式(2)模拟生成的湍流随机相位图。结构常数 C_n^2 在 $[1 \times 10^{-14}, 1 \times 10^{-13}]$ 范围内以 0.5×10^{-14} 为间隔均匀取值。除训练集外,每一种方案均另外设置了 5 组不同湍流强度 ($C_n^2 = 1 \times 10^{-14}, 2.5 \times 10^{-14}, 5 \times 10^{-14}, 7.5 \times 10^{-14}, 1 \times 10^{-13} \text{ m}^{-2/3}$) 的测试样本,以验证所设计的 CNN 的泛化能力。此外,每组由 1000 个测试样本组成。表 1 为数据集样本参数。

光束和湍流参数设置为: $p=0, l=5$,束腰半径为 30 mm,波长 $\lambda=1550 \text{ nm}$,栅格间距 $\Delta L=0.025 \text{ m}$,大气湍流内尺寸和外尺寸分别为 $l_0=0.0001 \text{ m}$ 和 $L_0=50 \text{ m}$, $N=64$,传输距离 $\Delta z=500 \text{ m}$ 。

3.3 仿真结果及讨论

图 7 是从每组测试集中随机选取的仿真相位图及其对应的预测相位图。

使用 MSE 衡量整体预测结果,给出的 MSE 值 (V_{MSE})为各组测试集 1000 样本的平均值:

$$V_{\text{MSE}} = \frac{1}{N^2} \sum_{q=1}^N \sum_{p=1}^N (f'_{qp} - f_{qp})^2, \quad (8)$$

式中: f'_{qp} 和 f_{qp} 分别为预测相位屏和仿真相位屏在空间坐标 (q, p) 处的灰度值。

表 2 列出了分别采用高斯探测光束和不采用高斯探测光束时预测的相位屏与模拟相位屏的 MSE,可以看到在 C_n^2 为 1×10^{-14} 和 $2.5 \times 10^{-14} \text{ m}^{-2/3}$ 时使用 GB, MSE 更小,说明预测结果更准确。随着 C_n^2 的不断增

表 1 数据集
Table 1 Database

| Data set | $C_n^2 / (10^{-14} \text{ m}^{-2/3})$ of LG | Sample size of LG | $C_n^2 / (10^{-14} \text{ m}^{-2/3})$ of GB | Sample size of LG |
|------------|---|-------------------|---|-------------------|
| Train set | [1, 10] | 30000 | [1, 10] | 30000 |
| Test set 1 | 1 | 1000 | 1 | 1000 |
| Test set 2 | 2.5 | 1000 | 2.5 | 1000 |
| Test set 3 | 5 | 1000 | 5 | 1000 |
| Test set 4 | 7.5 | 1000 | 7.5 | 1000 |
| Test set 5 | 10 | 1000 | 10 | 1000 |

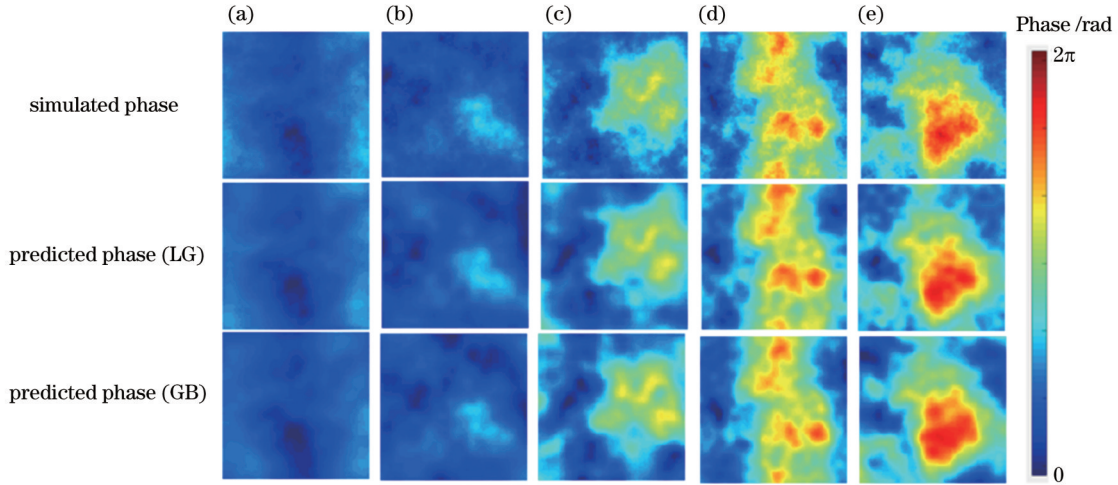


图 7 不同湍流强度下的模拟相位屏与预测相位屏。(a) $1 \times 10^{-14} \text{ m}^{-2/3}$; (b) $2.5 \times 10^{-14} \text{ m}^{-2/3}$; (c) $5 \times 10^{-14} \text{ m}^{-2/3}$; (d) $7.5 \times 10^{-14} \text{ m}^{-2/3}$; (e) $1 \times 10^{-13} \text{ m}^{-2/3}$
Fig. 7 Simulated and predicted phase screens with different turbulence intensities. (a) $1 \times 10^{-14} \text{ m}^{-2/3}$; (b) $2.5 \times 10^{-14} \text{ m}^{-2/3}$; (c) $5 \times 10^{-14} \text{ m}^{-2/3}$; (d) $7.5 \times 10^{-14} \text{ m}^{-2/3}$; (e) $1 \times 10^{-13} \text{ m}^{-2/3}$

大,使用对湍流更加敏感的 LG 光束来预测相位结果则更加准确, MSE 更小。

表 2 预测相位屏与模拟相位屏的 MSE 对比

Table 2 Comparison of MSE between predicted phase screen and simulated phase screen

| $C_n^2 / (10^{-14} \text{ m}^{-2/3})$ | 1 | 2.5 | 5 | 7.5 | 10 |
|---------------------------------------|------|------|------|------|------|
| MSE of LG | 0.07 | 0.15 | 0.25 | 0.38 | 0.53 |
| MSE of GB | 0.06 | 0.14 | 0.31 | 0.48 | 0.67 |

设 DPEnet 预测出的相位扰动为 $\tilde{\varphi}(x, y)$, 补偿后的电场函数 $\tilde{U}(z + \Delta z, x, y)$ 为

$$\tilde{U}(z + \Delta z, x, y) \approx \text{FFT}^{-1} \left\{ \exp \left\{ -i\Delta z \left[k_x^2 + k_y^2 / (2k_0) \right] \right\} \text{FFT} \left[U(z, x, y) \right] \right\} \times \exp \left[i\varphi(x, y) \right] \exp \left[-i\tilde{\varphi}(x, y) \right]. \quad (9)$$

图 8 给出了一个补偿的例子。显然, 经过补偿后, 畸变光束得到了明显改善。图 9 为校正前后模式纯度对比。表 3 列出了补偿前后光强图与源平面上 LG 光束光强图像的 MSE。校正后模式纯度有了明显提高,

MSE 有了明显的下降。两种方案都有效地校正了畸变相位, 提高了 LG 的纯度。随着 C_n^2 的增加, 相比于使用高斯光束, 使用 LG 得到的预测结果更好。在 $C_n^2 = 1 \times 10^{-13} \text{ m}^{-2/3}$ 时, 补偿后的模式纯度达到 96.8%, MSE 由补偿前的 1557.9 下降到 228.9。而使用 GB 训练补偿后模式纯度也达到 95.2%, MSE 下降到 243.1。图 10 为补偿前后的相位对比。图 10(a) 为源平面相位图, 图 10(b)~(f) 分别为 5 种不同湍流强度下未补偿与补偿后的相位图。可以看到, 补偿后的相位有了明显的校正。

4 结 论

提出一种基于 DPEnet 的相位预测算法, 以补偿由大气湍流引起的光束相位畸变, 校正接收端的光强分布, 提高通信的可靠性。DPEnet 经过训练自动学习输入样本光强分布与湍流扰动相位之间的映射关系, 输出预测相位。根据预测相位实现对涡旋光束的相位补偿。分别研究了使用高斯探测光束和不使用高斯探测光束两种方案的补偿效果, 在 5 种不同湍流强度测试下, 两种方案补偿后的模式纯度均达到 95% 以上, 补偿后图像与源场光强图像的均方误差均有明显下

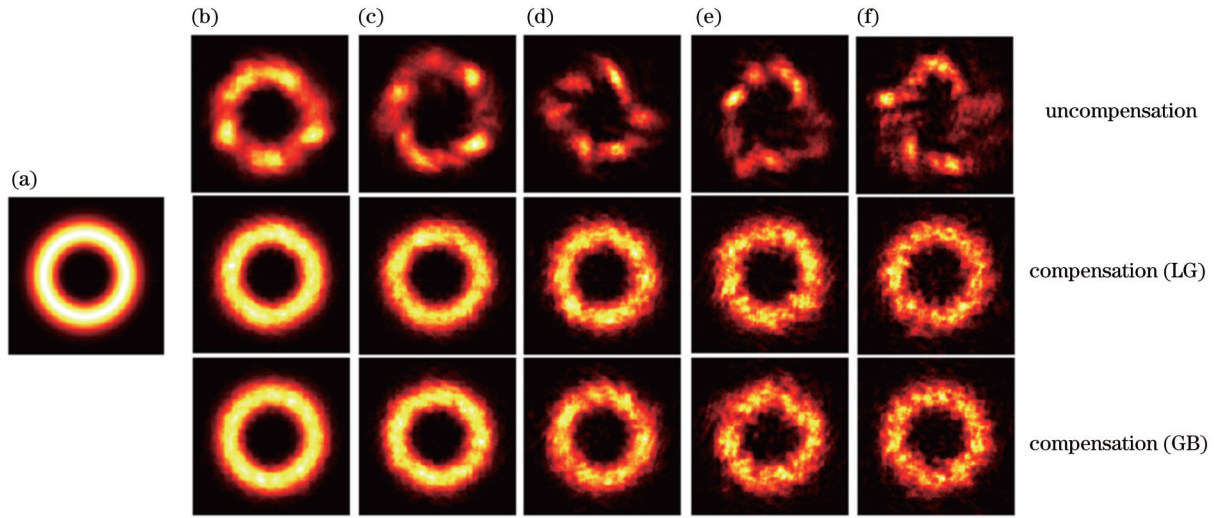


图 8 补偿结果。(a)源平面上的光强图;湍流强度分别为(b) $1 \times 10^{-14} \text{ m}^{-2/3}$ 、(c) $2.5 \times 10^{-14} \text{ m}^{-2/3}$ 、(d) $5 \times 10^{-14} \text{ m}^{-2/3}$ 、(e) $7.5 \times 10^{-14} \text{ m}^{-2/3}$ 、(f) $1 \times 10^{-13} \text{ m}^{-2/3}$ 时的未补偿与补偿后的光强图

Fig. 8 Compensation results. (a) Intensity profile in source plane; uncompensated and compensated intensity profiles with turbulence intensities of (b) $1 \times 10^{-14} \text{ m}^{-2/3}$, (c) $2.5 \times 10^{-14} \text{ m}^{-2/3}$, (d) $5 \times 10^{-14} \text{ m}^{-2/3}$, (e) $7.5 \times 10^{-14} \text{ m}^{-2/3}$, and (f) $1 \times 10^{-13} \text{ m}^{-2/3}$, respectively

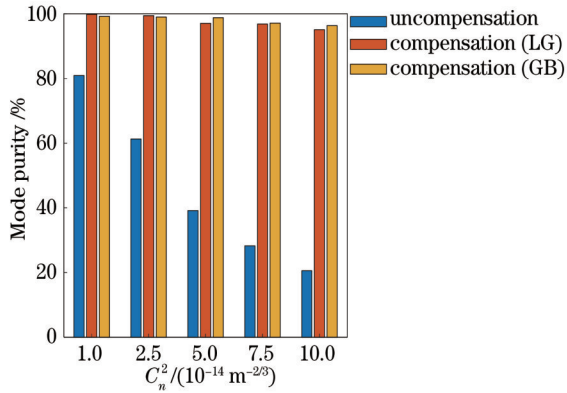


图 9 校正前后的模式纯度

Fig. 9 Mode purity before and after compensation

表 3 校正前后光强图 MSE 对比

Table 3 Comparison of MSE of intensity profiles before and after compensation

| $C_n^2 / (10^{-14} \text{ m}^{-2/3})$ | MSE without compensation | MSE with compensation for LG | MSE with compensation for GB |
|---------------------------------------|--------------------------|------------------------------|------------------------------|
| 1 | 246.8 | 50.3 | 48.4 |
| 2.5 | 527.8 | 68.1 | 64.1 |
| 5 | 931.3 | 98.9 | 109.0 |
| 7.5 | 1259.0 | 151.9 | 166.5 |
| 10 | 1557.9 | 228.9 | 243.1 |

降。即使在 $C_n^2 = 1 \times 10^{-13} \text{ m}^{-2/3}$ 、传输距离为 500 m 的

情况下,使用 DPEnet 的预测结果进行补偿后,两种方案的模式纯度分别从 20.5% 提高到 95.2% 和

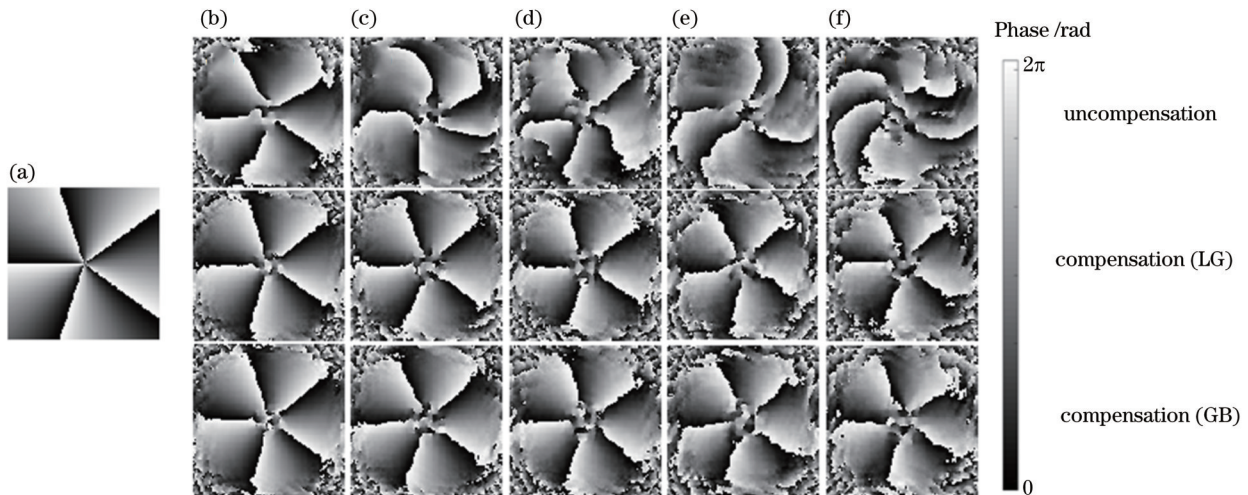


图 10 校正前后的相位。(a)源平面上的相位图;湍流强度分别为(b) $1 \times 10^{-14} \text{ m}^{-2/3}$ 、(c) $2.5 \times 10^{-14} \text{ m}^{-2/3}$ 、(d) $5 \times 10^{-14} \text{ m}^{-2/3}$ 、(e) $7.5 \times 10^{-14} \text{ m}^{-2/3}$ 、(f) $1 \times 10^{-13} \text{ m}^{-2/3}$ 时的未补偿与补偿后的相位图

Fig. 10 Phases before and after compensation. (a) Phase in source plane; uncompensated and compensated phases with turbulence intensities of (b) $1 \times 10^{-14} \text{ m}^{-2/3}$, (c) $2.5 \times 10^{-14} \text{ m}^{-2/3}$, (d) $5 \times 10^{-14} \text{ m}^{-2/3}$, (e) $7.5 \times 10^{-14} \text{ m}^{-2/3}$, and (f) $1 \times 10^{-13} \text{ m}^{-2/3}$, respectively

96.8%, MSE 由补偿前的 1557.9 分别下降到 228.9 和 243.1。结果表明,随着 C_n^2 逐渐变大,使用 LG 进行预测得到的结果更好。综上表明所提出的网络模型的预测结果可靠,补偿性能较好。

在未来的工作中,为了更好地达到相位校正效果,可以通过实验构建真实湍流环境,获得真实的训练样本。对相位校正过的涡旋光束进行编码传输,可大大提高通信的可靠性。

参 考 文 献

- [1] Shen Y J, Wang X J, Xie Z W, et al. Optical vortices 30 years on: OAM manipulation from topological charge to multiple singularities[J]. *Light: Science & Applications*, 2019, 8: 90.
- [2] Bai Y H, Lü H R, Fu X, et al. Vortex beam: generation and detection of orbital angular momentum[J]. *Chinese Optics Letters*, 2022, 20(1): 012601.
- [3] Bozinovic N, Yue Y, Ren Y X, et al. Terabit-scale orbital angular momentum mode division multiplexing in fibers[J]. *Science*, 2013, 340(6140): 1545-1548.
- [4] 南久航, 韩一平. 双路多进制涡旋光通信[J]. *光学学报*, 2021, 41(12): 1206001.
Nan J H, Han Y P. Dual-channel multiband vortex optical communication[J]. *Acta Optica Sinica*, 2021, 41(12): 1206001.
- [5] Trichili A, Salem A B, Dudley A, et al. Encoding information using Laguerre Gaussian modes over free space turbulence media[J]. *Optics Letters*, 2016, 41(13): 3086-3089.
- [6] Qiao Z, Wan Z Y, Xie G Q, et al. Multi-vortex laser enabling spatial and temporal encoding[J]. *Photonix*, 2020, 1(1): 13.
- [7] Li S H, Chen S, Gao C Q, et al. Atmospheric turbulence compensation in orbital angular momentum communications: advances and perspectives[J]. *Optics Communications*, 2018, 408: 68-81.
- [8] Li J, Zhang M, Wang D S, et al. Joint atmospheric turbulence detection and adaptive demodulation technique using the CNN for the OAM-FSO communication[J]. *Optics Express*, 2018, 26(8): 10494-10508.
- [9] Yuan Y S, Lei T, Gao S C, et al. The orbital angular momentum spreading for cylindrical vector beams in turbulent atmosphere[J]. *IEEE Photonics Journal*, 2017, 9(2): 6100610.
- [10] Zhao H, Deng W C, Li J, et al. Modified Gerchberg-Saxton algorithm-based probe-free wavefront distortion compensation of an OAM beam[J]. *Optik*, 2022, 269: 169816.
- [11] Fu S Y, Zhang S K, Wang T L, et al. Pre-turbulence compensation of orbital angular momentum beams based on a probe and the Gerchberg-Saxton algorithm[J]. *Optics Letters*, 2016, 41(14): 3185-3188.
- [12] Vorontsov M A, Sivokon V P. Stochastic parallel-gradient-descent technique for high-resolution wave-front phase-distortion correction[J]. *Journal of the Optical Society of America A*, 1998, 15(10): 2745-2758.
- [13] Xie G D, Ren Y X, Huang H, et al. Phase correction for a distorted orbital angular momentum beam using a Zernike polynomials-based stochastic-parallel-gradient-descent algorithm[J]. *Optics Letters*, 2015, 40(7): 1197-1200.
- [14] 马圣杰, 郝士琦, 赵青松. 基于改进型 SPGD 算法的涡旋光波前畸变校正[J]. *光学学报*, 2021, 41(6): 0601001.
Ma S J, Hao S Q, Zhao Q S. Wavefront distortion correction of vortex beam based on improved SPGD algorithm[J]. *Acta Optica Sinica*, 2021, 41(6): 0601001.
- [15] Zhou H P, Pan Z Z, Dedo M I, et al. High-efficiency and high-precision identification of transmitting orbital angular momentum modes in atmospheric turbulence based on an improved convolutional neural network[J]. *Journal of Optics*, 2021, 23(6): 065701.
- [16] 刘雪莲, 陈旭东, 林志立, 等. 深度学习辅助测量强散射涡旋光束拓扑荷数[J]. *光学学报*, 2022, 42(14): 1426001.
Liu X L, Chen X D, Lin Z L, et al. Deep-learning-assisted detection for topological charges of vortex beams through strong scattering medium[J]. *Acta Optica Sinica*, 2022, 42(14): 1426001.
- [17] Yin X L, Chen X Z, Chang H, et al. Experimental study of atmospheric turbulence detection using an orbital angular momentum beam via a convolutional neural network[J]. *IEEE Access*, 2019, 7: 184235-184241.
- [18] 叶玉儿, 李军依, 曹萌, 等. 双模式涡旋光束的轨道角动量的精确识别[J]. *激光与光电子学进展*, 2021, 58(18): 1811021.
Ye Y E, Li J Y, Cao M, et al. Accuracy recognition of orbital angular momentum of dual-mode vortex beams[J]. *Laser & Optoelectronics Progress*, 2021, 58(18): 1811021.
- [19] Ke X Z, Chen M. Recognition of orbital angular momentum vortex beam based on convolutional neural network[J]. *Microwave and Optical Technology Letters*, 2021, 63(7): 1960-1964.
- [20] Hao Y, Zhao L, Huang T, et al. High-accuracy recognition of orbital angular momentum modes propagated in atmospheric turbulences based on deep learning[J]. *IEEE Access*, 2020, 8: 159542-159551.
- [21] Wang Z K, Dedo M I, Guo K, et al. Efficient recognition of the propagated orbital angular momentum modes in turbulences with the convolutional neural network[J]. *IEEE Photonics Journal*, 2019, 11(3): 7903614.
- [22] Liu J M, Wang P P, Zhang X K, et al. Deep learning based atmospheric turbulence compensation for orbital angular momentum beam distortion and communication[J]. *Optics Express*, 2019, 27(12): 16671-16688.
- [23] Xiong W J, Wang P P, Cheng M L, et al. Convolutional neural network based atmospheric turbulence compensation for optical orbital angular momentum multiplexing[J]. *Journal of Lightwave Technology*, 2020, 38(7): 1712-1721.
- [24] Hill R J. Models of the scalar spectrum for turbulent advection[J]. *Journal of Fluid Mechanics*, 1978, 88(3): 541-562.
- [25] Andrews L C, Phillips R L. *Laser beam propagation through random media*[M]. Bellingham: SPIE Press, 2005.
- [26] 骆传凯, 卢芳, 苗志芳, 等. 径向阵列涡旋光束在大气中的传输与扩展[J]. *光学学报*, 2019, 39(6): 0601004.
Luo C K, Lu F, Miao Z F, et al. Propagation and spreading of radial vortex beam array in atmosphere[J]. *Acta Optica Sinica*, 2019, 39(6): 0601004.
- [27] Guo J W, Shi H Y, Yang T, et al. Atmospheric turbulence compensation for OAM-carrying vortex waves based on convolutional neural network[J]. *Advances in Space Research*, 2022, 69(5): 1949-1959.
- [28] Lohani S, Glasser R T. Turbulence correction with artificial neural networks[J]. *Optics Letters*, 2018, 43(11): 2611-2614.
- [29] Hou T Y, An Y, Chang Q, et al. Deep-learning-assisted, two-stage phase control method for high-power mode-programmable orbital angular momentum beam generation[J]. *Photonics Research*, 2020, 8(5): 715-722.
- [30] Wang X Y, Wu T Y, Dong C, et al. Integrating deep learning to achieve phase compensation for free-space orbital-angular-momentum-encoded quantum key distribution under atmospheric turbulence[J]. *Photonics Research*, 2021, 9(2): B9-B17.

Vortex Beam Phase Correction Based on Deep Phase Estimation Network

Liu Juan, Du Qian, Liu Fangning, Wang Ke, Yu Jiayi^{**}, Wei Dongmei^{*}

Shandong Provincial Engineering and Technical Center of Light Manipulations, School of Physics and Electronics, Shandong Normal University, Jinan 250358, Shandong, China

Abstract

Objective Vortex beams carry orbital angular momentum and have a phase factor $\exp(i l \theta)$, where l is the topological charge number and θ is direction angle. Theoretically, l can take any integer value, and different orbital angular momentum modes are mutually orthogonal. Therefore, in optical communication, the orbital angular momentum can be used for information transmission and exchange or multiplexed to improve communication capacity. However, vortex beams are affected by turbulence when transmitting in atmospheric turbulence, which results in the distortion of their spiral phase and causes inter-mode crosstalk and reduced communication reliability. Many studies focus on compensating the phase distortion of vortex beams, with adaptive optics systems commonly used. However, such methods require multiple iterations, converge slowly, and easily fall into local minima. In recent years, convolutional neural networks have attracted extensive attention in various fields due to their powerful image processing capabilities. Therefore, in this paper, convolutional neural networks are used to extract atmospheric turbulence information from distorted light intensity distribution and recover its distortion. This deep learning-based compensation method has even more accurate and faster correction capability than adaptive optics systems. In view of this, convolutional neural networks are employed herein for the phase prediction of atmospheric turbulence to achieve the phase compensation of Laguerre-Gaussian (LG) beams and improve modal detection accuracy and communication reliability.

Methods In this paper, a novel convolutional neural network, i. e. , deep phase estimation network, is constructed to achieve the prediction of turbulent phases. With this proposed deep network, a mapping between light intensity and turbulent phase caused by atmospheric turbulence is established. Here two strategies are used for learning and predicting the turbulent phase respectively: one uses a Gaussian beam as the probe beam, and the other makes a direct prediction with an LG beam carrying information without a probe beam. In the target plane, the turbulent phase is predicted by intensity, and the field is corrected by the predicted phase. The inputs of the networks of the two schemes are a Gaussian beam and an LG beam, respectively, and the output is the corresponding predicted phase of atmospheric turbulence. The deep phase estimation network performs feature extraction of the input light intensity profile by under-sampling through the encoder, learns the atmospheric turbulence feature parameters by up-sampling through the decoder to achieve the reconstruction of the equivalent atmospheric turbulence phase screen, and finally outputs the results. By learning and training a large number of samples, the network structure proposed in this paper can achieve good prediction results at a transmission distance of 500 m. In addition, five sets of intensity profiles with different turbulence intensities are set for testing and verifying the network to prove that the network has strong generalization ability. Then, the compensation is achieved by loading the reverse phase of the predicted phase on the distorted beam to exert the correction effect.

Results and Discussions In this paper, we construct a deep phase estimation network consisting of 15 convolutional layers, 3 deconvolutional layers, and 3 skip connections (Fig. 6) by using an encoder-decoder architecture, which can achieve phase prediction at long transmission distances. At a transmission distance of 500 m, after the network is trained with the distorted beam at different turbulence intensities, it can predict the turbulence phase screen with a high agreement with the simulation results of tests at five different turbulence intensities (Fig. 7). The prediction results are evaluated by calculating the mean square error between them and the simulation results, and it is found that the network can effectively extract turbulence information and has strong generalization ability (Table 2). The beam phase correction is achieved by loading the predicted phase reverse to the distorted beam, and the intensity profile (Fig. 8) and phase (Fig. 10) are corrected to a large extent. The mode purity of the corrected beam is greatly improved, and the mean square error of the intensity image is significantly reduced (Table 3).

Conclusions The results show that the deep phase estimation network created in this paper can achieve phase prediction more accurately, and it is trained to automatically learn the mapping relationship between the input sample light intensity distribution and the turbulent phase and output the predicted phase. The phase compensation of the vortex beam is achieved based on the predicted phase. The compensation effects of two schemes using a Gaussian probe beam and not using a probe beam are investigated separately, and both of them are effective in correcting the distorted phase. They can

predict the turbulent phase accurately under tests at five different turbulent intensities. After compensation, the mode purity of the beam reaches more than 95%, and the mean square errors of the compensated light intensity image and the source plane are both significantly reduced. Even in the case of $C_n^2 = 1 \times 10^{-13} \text{ m}^{-2/3}$ and transmission distance of 500 m, the mode purity of the two schemes is improved from 20.5% to 95.2% and 96.8%, respectively, after the compensation of the prediction results with the deep phase estimation network, and the mean square error also decreases significantly. In summary, the prediction results of the network model proposed in this paper are reliable, and the compensation performance is good.

Key words atmospheric optics; vortex beam; convolutional neural network; phase prediction; atmospheric turbulence